

THE SCUBA-2 850 μm FOLLOW-UP OF WISE-SELECTED, LUMINOUS DUST-OBSCURED QUASARS

LULU FAN,¹ SUZY F. JONES,² YUNKUN HAN,³ AND KIRSTEN K. KNUDSEN²

¹*Shandong Provincial Key Lab of Optical Astronomy and Solar-Terrestrial Environment, Institute of Space Science, Shandong University, Weihai, 264209, China*

²*Department of Space, Earth and Environment, Chalmers University of Technology, Onsala Space Observatory, SE-439 92 Onsala, Sweden*

³*Yunnan Observatories, Chinese Academy of Sciences, Kunming, 650011, China*

ABSTRACT

Hot dust-obscured galaxies (Hot DOGs) are a new population recently discovered in the *WISE* All-Sky survey. Multiwavelength follow-up observations suggest that they are luminous, dust-obscured quasars at high redshift. Here we present the JCMT SCUBA-2 850 μm follow-up observations of 10 Hot DOGs. Four out of ten Hot DOGs have been detected at $> 3\sigma$ level. Based on the IR SED decomposition approach, we derive the IR luminosities of AGN torus and cold dust components. Hot DOGs in our sample are extremely luminous with most of them having $L_{\text{IR}}^{\text{tot}} > 10^{14} L_{\odot}$. The torus emissions dominate the total IR energy output. However, the cold dust contribution is still non-negligible, with the fraction of the cold dust contribution to the total IR luminosity ($\sim 8 - 24\%$) being dependent on the choice of torus model. The derived cold dust temperatures in Hot DOGs are comparable to those in UV bright quasars with similar IR luminosity, but much higher than those in SMGs. Higher dust temperatures in Hot DOGs may be due to the more intense radiation field caused by intense starburst and obscured AGN activities. Fourteen and five submillimeter serendipitous sources in the 10 SCUBA-2 fields around Hot DOGs have been detected at $> 3\sigma$ and

$> 3.5\sigma$ levels, respectively. By estimating their cumulative number counts, we confirm the previous argument that Hot DOGs lie in dense environments. Our results support the scenario in which Hot DOGs are luminous, dust-obscured quasars lying in dense environments, and being in the transition phase between extreme starburst and UV-bright quasars.

Keywords: galaxies: evolution - galaxies: active - infrared: galaxies - submillimeter:
galaxies - quasars: general

1. INTRODUCTION

Massive galaxies have been thought to co-evolve with their central supermassive black holes (Alexander & Hickox 2012; Kormendy & Ho 2013). In the co-evolution scenario, starburst galaxies, such as ultraluminous infrared galaxies (ULIRGs; Sanders & Mirabel 1996) and sub-millimeter galaxies (SMGs; Blain et al. 2002; Casey et al. 2014), ultraviolet (UV) bright quasars (QSOs) and massive early-type galaxies (ETGs) have been proposed to form an evolutionary sequence (Sanders et al. 1988; Hopkins et al. 2008). Luminous dust-obscured QSOs represent a brief transition phase from starburst galaxies to unobscured QSOs. It is important to understand this obscured phase, especially at $z \sim 2 - 3$ when both cosmic star formation and black-hole growth reach their peaks (Reddy et al. 2008; Brandt & Alexander 2015). However, it is not easy to select large samples of obscured QSOs in the normal UV/optical and X-ray surveys due to dust obscuration. Dust absorbs the UV and optical radiations from star formation and the black-hole accretion disk, and re-emits at far-IR/(sub-)mm wavelengths, making them be very luminous in the IR but faint at UV and optical wavelengths.

NASA's *Wide-field Infrared Survey Explorer* (*WISE* ; Wright et al. 2010) performed an all-sky survey with images in four mid-IR bands ($W1$, $W2$, $W3$ and $W4$) at wavelengths of $3.4 \mu m$, $4.6 \mu m$, $12 \mu m$ and $22 \mu m$, providing the sensitivity to detect luminous dust-obscured QSOs. One of the primary science objectives for *WISE* is to identify the most luminous ULIRGs in the Universe. In order to achieve this goal, a new color-selected method (so-called $W1W2$ -dropouts) with all *WISE* four bands has been recently introduced and proven to be very successful (Eisenhardt et al. 2012; Wu et al. 2012). This method searched the luminous dust-obscured galaxies, which are prominent in the *WISE* 12 or $22 \mu m$ bands, and faint or undetected in the 3.4 and $4.6 \mu m$ bands. Spectroscopic follow-up of about 150 galaxies selected with this method have shown that most of them are at redshift from 1 to 4 (Tsai et al. 2015; Assef et al. 2015). Given bright $W3/W4$ bands and high redshift, these galaxies should have very high mid-IR luminosities.

Various follow-up studies have provided additional aspects on understanding the physical properties of this population. Together with *WISE* photometry, continuum measurements at longer wavelengths with the *Herschel* Space Observatory (Pilbratt et al. 2010) PACS (Photodetector Array Camera and

Spectrometer; Poglitsch et al. 2010) observations at 70 and 160 μm and SPIRE (Spectral and Photometric Imaging REceiver; Griffin et al. 2010) observations at 250, 350, and 500 μm (PI: P.R.M. Eisenhardt), the CSO (Caltech Submillimeter Observatory) SHARC-II and Bolocam observations at 350, 450, 850 and 1100 μm (Wu et al. 2012) and the SCUBA-2 (Submillimeter Common-User Bolometer Array) 850 μm observations (Jones et al. 2014) provide the full IR spectral energy distributions (SEDs) of tens of these galaxies, which suggest that (1) they are indeed hyper-luminous with $L_{\text{bol}} > 10^{13}L_{\odot}$ and even extremely luminous with $L_{\text{bol}} > 10^{14}L_{\odot}$ (Tsai et al. 2015); (2) their IR luminosities are dominated by hot dust radiation which is heated by active galactic nuclei (AGN) instead of star formation. The mid-IR bright criterion is very similar to that of dust-obscured galaxies (DOGs; Dey et al. 2008). Following the terminology of Wu et al. (2012), these galaxies have been referred as hot, dust-obscured galaxies (Hot DOGs). The detailed IR SED decomposition confirmed that Hot DOGs have both extreme AGN and starburst activities and hot dust emission from AGN torus dominates the IR energy output (Fan et al. 2016b). Recent X-ray observations of several Hot DOGs with XMM-Newton, Chandra and NuSTAR (Stern et al. 2014; Assef et al. 2016; Piconcelli et al. 2015; Ricci et al. 2017) revealed that they are likely heavily dust-obscured, possibly Compton-thick AGN.

Both extreme AGN and starburst activities in Hot DOGs are likely triggered by major mergers, which has been suggested by the recent studies of the high resolution HST WFC3 NIR imaging (Fan et al. 2016a; but also see Farrah et al. 2017 for an opposite conclusion) and ALMA CO line imaging (Fan et al. 2017 in prep). Wu et al. (2017) measured the supermassive black hole (SMBH) masses via broad H_{α} emission lines, using Keck/MOSFIRE and Gemini/FLAMINGOS-2. They found substantial corresponding SMBH masses for these Hot DOGs ($\sim 10^9M_{\odot}$), and their derived Eddington ratios are close to unity (see also the similar results in Lonsdale et al. 2015 for a radio-selected Hot DOG sample). A recent ALMA [CII] observation of the most luminous Hot DOG W2246–0526 revealed an extended and highly turbulent ISM, arguing that it is blowing out its ISM isotropically (Díaz-Santos et al. 2016). Given the major-merger triggering scenario, high luminosities, high SMBH masses, high Eddington ratios and strong feedback, Hot DOGs, as luminous

dust-obscured QSOs, are suggested to be in a key transition phase of massive galaxy evolution, linking starbursts and luminous unobscured quasars (Wu et al. 2012; Bridge et al. 2013; Díaz-Santos et al. 2016; Fan et al. 2016b; Wu et al. 2017).

Despite the dominance of AGN torus emission, cold dust emission related to star formation is non-negligible (Wu et al. 2012; Fan et al. 2016b). Constraining the contribution of cold dust emission will be very important to help understanding the co-growth of galaxy and SMBH during the dust-obscured phase. In this work, we present James Clerk Maxwell Telescope (JCMT) SCUBA-2 850 μm observations of ten Hot DOGs. With these long wavelength measurements, we try to constrain the contribution of cold dust emission compared to the AGN torus emission and study the SMG environment around Hot DOGs. In Section 2, we describe the sample selection, observations and data analysis. We introduce the IR SED decomposition method with two different model sets in Section 3. In Section 4, we present the results of IR SED fitting and the environmental studies around Hot DOGs. We discuss and summarize the results in Section 5 and Section 6, respectively. Throughout this work we assume a standard, flat Λ CDM cosmology (Komatsu et al. 2011), with $H_0 = 70 \text{ km s}^{-1}$, $\Omega_M = 0.3$, and $\Omega_\Lambda = 0.7$.

2. DATA AND SAMPLE SELECTION

2.1. Sample selection

The ten Hot DOGs reported here are selected from the *WISE* All-Sky Source catalog, which provides point-spread function-fitting magnitudes and uncertainties of four mid-IR bands ($W1$, $W2$, $W3$ and $W4$) at wavelengths of 3.4 μm , 4.6 μm , 12 μm and 22 μm (Wright et al. 2010; Cutri et al. 2013). The basic idea of Hot DOGs selection is to target those mid-IR luminous galaxies with faint or undetected $W1/W2$ bands, and prominent $W3/W4$ bands. The selected galaxies have $W1 > 17.4$ ($< 34\mu\text{Jy}$) and either $W3 < 7.7$ ($> 6.9 \text{ mJy}$) and $W2 - W4 > 8.2$, or $W3 < 10.6$ ($> 1.7 \text{ mJy}$) and $W2 - W3 > 5.3$ (Eisenhardt et al. 2012; Wu et al. 2012).

For our purposes of SCUBA-2 follow-up, we required that the selected Hot DOGs: (1) had known spectroscopic redshift in the literature (Wu et al. 2012; Tsai et al. 2015). (2) had *Herschel* PACS

and SPIRE observations. By using these criteria, we selected nineteen Hot DOGs. Among them, ten Hot DOGs were randomly chosen to observe by SCUBA-2 according to the JCMT queue-based flexible observing system.

2.2. JCMT SCUBA-2 observations and photometry

Observations of the ten Hot DOGs were obtained using the JCMT SCUBA-2 camera, scheduled flexibly in 2015A and 2015B semesters (Program ID: M15AI06 and M15BI016), from 2015 April to 2016 June. During the observations, the precipitable water vapor (PWV) was in the range 2.0-3.0 mm, corresponding to the zenith atmospheric optical depth at 225 GHz: $0.08 < \tau_{225\text{GHz}} < 0.12$ and the extinction coefficients at 450 μm and 850 μm : $1.77 < \tau_{450} < 2.81$ and $0.35 < \tau_{850} < 0.53$ (Dempsey et al. 2013). Even if both 450 μm and 850 μm measurements were taken simultaneously, 450 μm data couldn't be used due to the high atmospheric opacity and noise levels.

All observations were carried out in SCAN mode using the so-called 'DAISY' pattern which provides a 12-arcminute-diameter map with uniform exposure-time coverage in the central 3-arcminute-diameter region. The full width at half maximum (FWHM) of the main beam at 850 μm is about 14.5 arcsecond (Holland et al. 2013). For seven out of ten targets, two hours of the total exposure time were spent, consisting of four separate 30-minutes-long scans. The remaining targets, W0134–2922, W0248+2705 and W0859+4823, had 150, 60 and 90 minutes exposure time, respectively. The calibration sources observed were Uranus and Mars, and also secondary calibrators from the James Clerk Maxwell Telescope (JCMT) calibrator list (Dempsey et al. 2013). Calibrations were taken before and after the target observations.

The SCUBA-2 maps were reduced using the Dynamic Iterative Map Maker (DIMM) within the STARLINK SubMillimeter User Reduction Facility (SMURF) data reduction package (Chapin et al. 2013). DIMM was used to produce a map for each 30-minutes-long scan by using mapmaker command with the 'Blank Field configuration' which is suitable for the faint point sources. Using the STARLINK Pipeline for Combining and Analyzing Reduced Deduced Data (PICARD) package, all maps for each target were mosaicked, cropped to a 90-arcsecond-radius circle, beam-match filtered

Table 1. SCUBA-2 observations and photometry of the 10 Hot DOGs.

Source	R.A.	Decl.	Redshift	Exposure time	UT Date	τ_{225GHz}	850 μm
Name	(J2000)	(J2000)		(hr)			(mJy)
W0126–0529	01:26:11.96	–05:29:09.6	2.937	2.0	2015 Nov 18, Dec 25-26	0.09,0.10	15.9 ± 2.6
W0134–2922	01:34:35.71	–29:22:45.4	3.047	2.5	2015 Dec 25,27 2016 Jan 7,Jun 4	0.09,0.10,0.12	$< 5.3^a$
W0248+2705	02:48:58.81	+27:05:29.8	2.210	1.0	2015 Dec 25	0.09	$< 5.5^a$
W0422–1028	04:22:48.82	–10:28:32.0	2.227	2.0	2015 Nov 10,18	0.10,0.09	$< 4.6^a$
W0757+5113	07:57:25.07	+51:13:19.7	2.277	2.0	2015 Oct 26-27	0.10,0.09	$< 4.7^a$
W0859+4823	08:59:29.94	+48:23:02.3	3.245	1.5	2015 Oct 27-28	0.09,0.08	7.0 ± 2.0
W1248–2154	12:48:15.21	–21:54:20.4	3.318	2.0	2015 May 12, Dec 25	0.09	$< 4.7^a$
W1838+3429	18:38:09.16	+34:29:25.9	3.205	2.0	2015 Jun 1-2, Jul 16	0.11,0.12,0.09	$< 5.2^a$
W2201+0226	22:01:23.39	+02:26:21.8	2.877	2.0	2015 May 26	0.10	17.2 ± 2.5
W2210–3507	22:10:11.87	–35:07:20.0	2.814	2.0	2015 Apr 25, May 31 2015 Jun 17, Jul 16	0.10, 0.09	12.3 ± 3.1

Notes.^a 2σ upper limits at 850 μm .

with a 15-arcsecond FWHM Gaussian and calibrated with the flux conversion factors (FCFs). We adopted the FCFs value of $537 \text{ Jy pW}^{-1} \text{ beam}^{-1}$ for $850 \mu\text{m}$ data (Dempsey et al. 2013).

In Table 1, we present the result of SCUBA-2 $850 \mu\text{m}$ photometry of the ten Hot DOGs. Four out of ten Hot DOGs (W0126–0529, W0859+4823, W2201+0226 and W2210–3507) have been detected at $> 3\sigma$ significance and their flux densities and uncertainties are included in Table 1. The remaining six Hot DOGs (W0134–2922, W0248+2705, W0422–1028, W0757+5113, W1248–2154 and W1838+3429) are undetected. Their 2σ upper limits have been presented in Table 1. The photometric method presented here is identical to that in Jones et al. (2014) towards a sub-sample of the same parent population of our targets. However, mainly due to the different observation conditions, our photometric results are slightly different from those in Jones et al. (2014). Our observations were in the range of JCMT Band 3 conditions while those of Jones et al. (2014) were in the better conditions (Band 2). The average 1σ depths reach 2.6 mJy and 1.8 mJy for our observations and Jones et al. (2014), respectively. Instead of 40% detection rate in our observations, a higher detection rate (60%) has been found in Jones et al. (2014).

2.3. Ancillary data

In order to construct the full infrared SED of the ten SCUBA-2 observed Hot DOGs, we combined the public *WISE* and *Herschel* photometry. We retrieved the *WISE* *W3* and *W4* photometry from the ALLWISE Data Release (Cutri et al. 2013). We used zero points of 29.04 and 8.284 Jy to convert *W3* and *W4* Vega magnitude to flux densities, respectively (Wright et al. 2010). All of the ten Hot DOGs in our sample had been observed by *Herschel* PACS (Poglitsch et al. 2010) at 70 and $160 \mu\text{m}$, and SPIRE (Griffin et al. 2010) at 250, 350 and $500 \mu\text{m}$. Both PACS and SPIRE data were retrieved from the Herschel Science Archive (HSA) and reduced using the Herschel Interactive Processing Environment (HIPE v14.2.1). The flux densities and uncertainties of PACS and SPIRE were measured using the identical method in Fan et al. (2016b).

3. IR SED FITTING

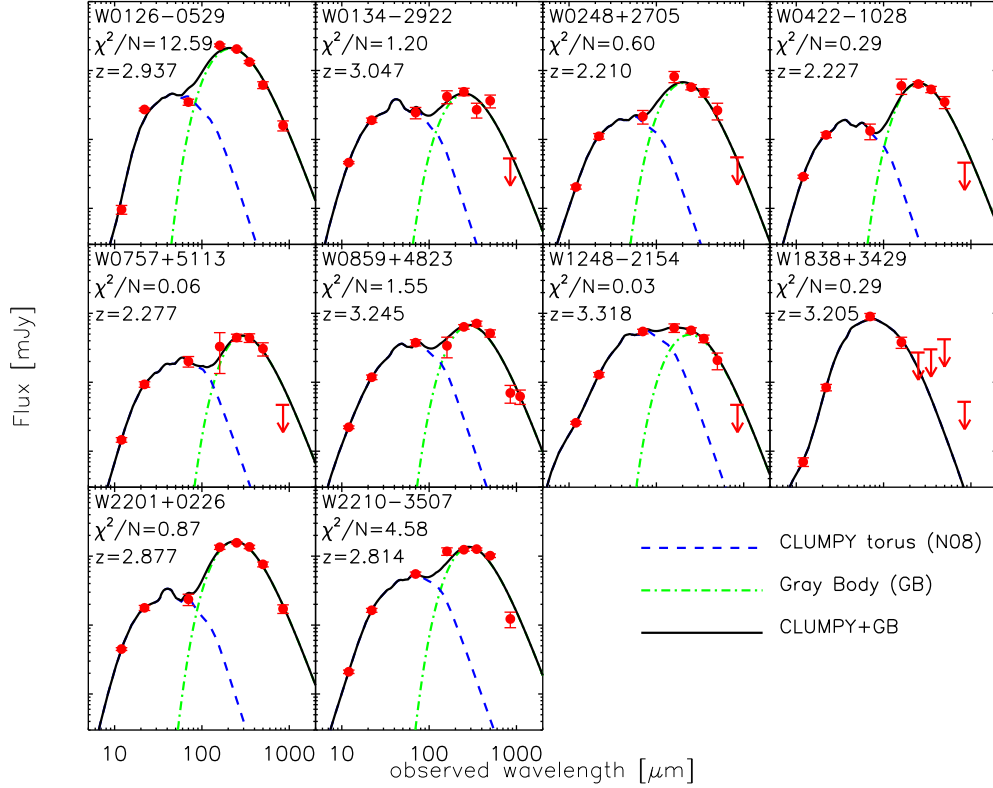


Figure 1. Best-fit model SEDs with the CLUMPY+GB model for the ten SCUBA-2 observed Hot DOGs in our sample. The filled circles represent the observed data points. The downward arrows mark the upper limits of undetected bands. The solid line represents the combined CLUMPY+GB model. The dashed and dot-dashed lines represent the components of the clumpy torus and gray body in the CLUMPY+GB model, respectively.

In this section, we describe how to fit the observed IR SEDs of the ten Hot DOGs. We assume that their IR SEDs are mainly distributed by two components. One is the hotter AGN heated dust emission and the other is colder young stellar population heated dust emission. It is obvious that the fitting results are dependent on which model is used for each component. For the AGN heated dust emission, we have employed two kinds of torus models: the CLUMPY torus model by [Nenkova et al.](#)

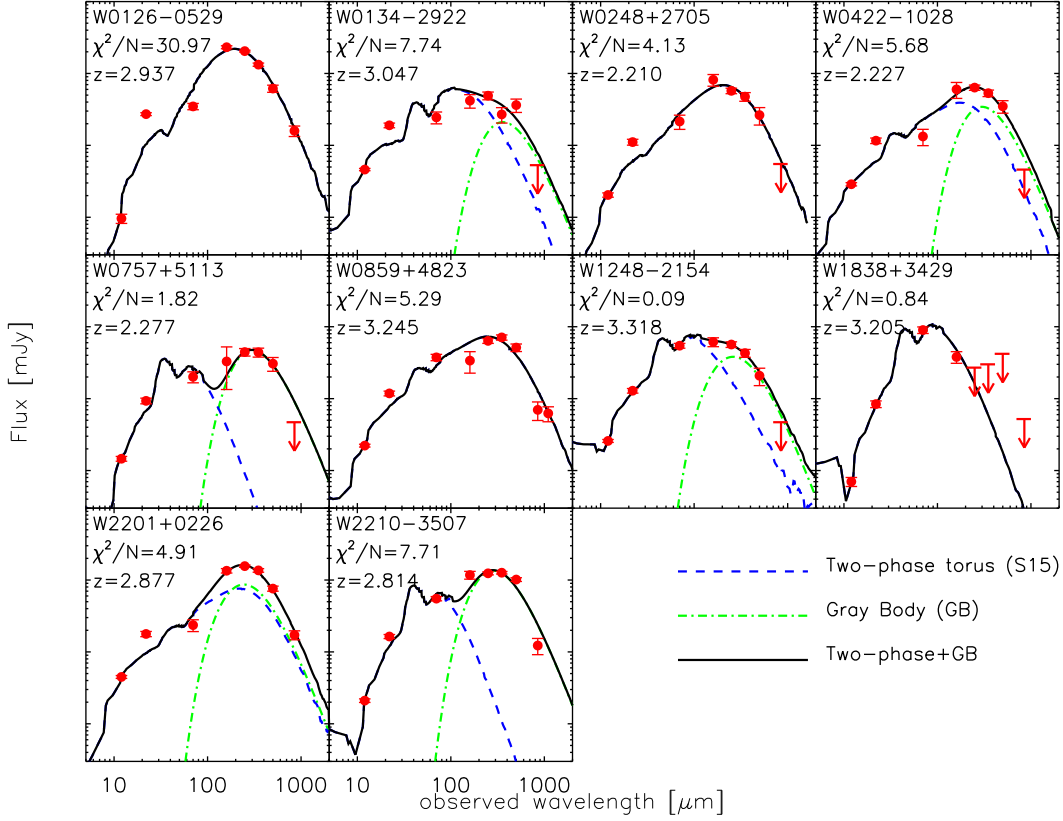


Figure 2. Best-fit model SEDs with the Two-phase+GB model for the ten SCUBA-2 observed Hot DOGs in our sample. The filled circles represent the observed data points. The downward arrows mark the upper limits of undetected bands. The solid line represents the combined Two-phase+GB model. The dashed and dot-dashed lines represent the components of the two-phase torus and gray body in the Two-phase+GB model, respectively.

(2002); [Nenkova et al. \(2008a,b\)](#)¹ and the two-phase torus model by [Siebenmorgen et al. \(2015\)](#). For the young stellar population heated dust emission, we have employed a simple modified blackbody model (or a gray body, GB).

¹ www.clumpy.org

For the CLUMPY torus model, we use the newly calculated model database². There are 6 free parameters in the CLUMPY torus model. We assume that the 6 free parameters have the uniform distributions within the following intervals: the number of clouds along a radial equatorial path $N_0 = [1, 15]$, the ratio of the outer to the inner radii of the toroidal distribution $Y = R_o/R_d = [5, 100]$, the viewing angle measured from the torus polar axis $i = [0, 90]$, the index $q = [0, 3]$ of the radial density profile r^{-q} , the width parameter characterizing the angular distribution $\sigma = [15, 70]$, and the effective optical depth of clumps $\tau_V = [10, 300]$. Given a set of parameter values, a model SED can be calculated. There are in total 1,247,400 model SEDs in the database.

For the two-phase torus model (Siebenmorgen et al. 2015), we use the provided SED library³. Unlike the CLUMPY torus model, the two-phase torus model assumes that torus dust is not only distributed in a clumpy medium, but also a homogeneous disk. The SED of two-phase torus model has been computed with a self-consistent three dimensional radiative transfer code, with a set of model parameters including the viewing angle, the inner radius, the volume filling factor, optical depth of the clouds and the optical depth of the disk mid-plane.

To represent the cold dust emission, we employ a gray body model, which is defined as:

$$S_\lambda \propto (1 - e^{-(\frac{\lambda_0}{\lambda})^\beta}) B_\lambda(T_{\text{dust}}) \quad (1)$$

where B_λ is the Planck blackbody spectrum, T_{dust} is dust temperature. We adopt $\lambda_0 = 125 \mu\text{m}$ and $\beta=1.6$, which are the typical values used for high redshift QSOs (Beelen et al. 2006; Wang et al. 2008, 2011). The dust temperature T_{dust} is set as a free parameter with a uniform prior truncated to the interval of $\log(T_{\text{dust}}/\text{K})=[1,2]$.

Adopting a combination of the CLUMPY or two-phase torus model and a gray body, we implement the IR SED decomposition of the ten Hot DOGs in our sample by using an updated version of the Bayesian SED fitting code, BayeSED (Han & Han 2012, 2014)⁴. BayeSED is designed to be a general purpose Bayesian SED fitting code. It can be used to fit the multiwavelength SEDs of galaxies with a

² http://www.pa.uky.edu/clumpy/models/clumpy_models_201410_tvavg.hdf5/

³ <http://www.eso.org/~rsiebenm/AGN/>

⁴ <https://bitbucket.org/hanyk/bayesed/>

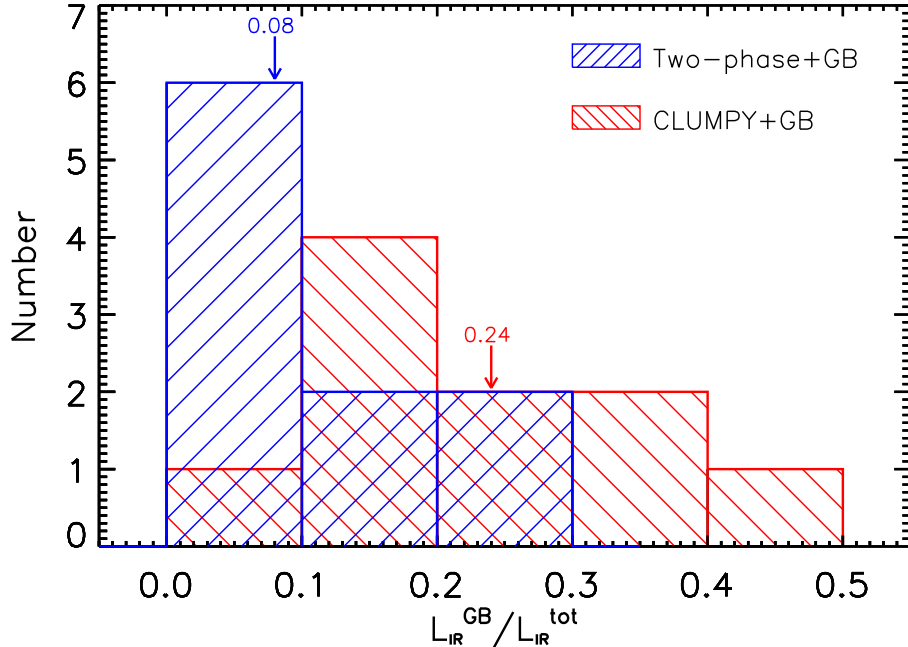


Figure 3. Distributions of the fraction of the cold dust emission to the total IR luminosity ($L_{\text{IR}}^{\text{GB}}/L_{\text{IR}}^{\text{tot}}$). The mean values of $L_{\text{IR}}^{\text{GB}}/L_{\text{IR}}^{\text{tot}}$ are 0.24 and 0.08 in the CLUMPY+GB model (red) and the Two-phase+GB model (blue), respectively.

combination of whatever SED models. A detailed description of BayeSED can be found in [Fan et al. \(2016b\)](#). Here we summarize several basic features of BayeSED. (1) By using principal component analysis (PCA), the SED library dimensionality can be reduced without sacrificing much accuracy. (2) The model SED at any position of the parameter space spanning the model SED library can be generated by employing a supervised machine learning method (K-Nearest Neighbors searching). (3) Instead of the traditional Markov Chain Monte Carlo (MCMC) algorithm, the multimodal nested sampling algorithm ([MultiNest](#), [Feroz & Hobson 2008](#); [Feroz et al. 2009](#)) has been employed to obtain the posterior probability distribution function (PDF) of parameters.

4. RESULTS

4.1. IR luminosities and dust temperatures

Table 2. Derived IR luminosities of Hot DOGs.

Source	CLUMPY torus + Gray body			Two-phase torus + Gray body		
	$\log L_{\text{IR}}^{\text{t}}$	$\log L_{\text{IR}}^{\text{GB}}$	$\log L_{\text{IR}}^{\text{tot}}$	$\log L_{\text{IR}}^{\text{t}}$	$\log L_{\text{IR}}^{\text{GB}}$	$\log L_{\text{IR}}^{\text{tot}}$
	(L_{\odot})	(L_{\odot})	(L_{\odot})	(L_{\odot})	(L_{\odot})	(L_{\odot})
W0126–0529	13.99±0.01	13.92±0.01	14.26±0.03	14.20±0.01	-	14.20±0.01
W0134–2922	14.02±0.02	13.20±0.05	14.08±0.08	14.07±0.17	12.68±0.48	14.10±0.65
W0248+2705	13.43±0.05	13.11±0.07	13.60±0.12	13.53±0.05	-	13.53±0.05
W0422–1028	13.45±0.03	13.01±0.05	13.58±0.08	13.52±0.09	12.64±0.34	13.58±0.43
W0757+5113	13.42±0.03	12.80±0.05	13.51±0.08	13.51±0.08	12.80±0.17	13.59±0.25
W0859+4823	13.99±0.02	13.36±0.03	14.08±0.05	14.04±0.06	-	14.04±0.06
W1248–2154	14.13±0.02	13.36±0.07	14.20±0.09	14.25±0.11	13.21±0.35	14.32±0.46
W1838+3429	14.16±0.02	-	14.16±0.02	14.24±0.19	-	14.24±0.19
W2201+0226	13.92±0.03	13.72±0.02	14.14±0.05	13.97±0.11	13.44±0.17	14.09±0.28
W2210–3507	13.97±0.02	13.50±0.02	14.10±0.04	14.04±0.04	13.52±0.03	14.16±0.07

In Figure 1, we present the best-fitting results with the CLUMPY+GB model for the ten SCUBA-2 observed Hot DOGs in our sample. Based on the best-fitting results of our IR SED decomposition approach, we can derive not only the total IR luminosities, but also the individual contributions of both torus (blue dashed line in Figure 1) and cold dust components (green dot-dashed line in Figure 1). In Table 2, we list the total IR luminosities ($L_{\text{IR}}^{\text{tot}}$), the IR luminosities emitted by the torus (L_{IR}^{t}) and cold dust ($L_{\text{IR}}^{\text{GB}}$), respectively. All of them are HyLIRGs (Hyper-luminous Infrared Galaxies) with $L_{\text{IR}}^{\text{tot}} > 10^{13}L_{\odot}$. Seven out of ten Hot DOGs are ELIRGs (Extremely Luminous Infrared Galaxies, Tsai et al. 2015) with $L_{\text{IR}}^{\text{tot}} > 10^{14}L_{\odot}$. The torus emissions contribute over half of the total IR energy output. However, all but one (W1838+3429) show the non-negligible IR luminosities ($10^{12.8-13.9}L_{\odot}$) emitted by cold dust, which contribute up to 50% of the total IR luminosities. The average fraction

of the cold dust to the total IR luminosities is 24% (see Figure 3). The results suggest that Hot DOGs contain both very powerful AGN and extreme starbursts with SFRs of several thousands solar masses per year.

The derived IR luminosities may depend on the adopted torus models. In Figure 2, we also present the best-fitting results with the Two-phase+GB model for the ten SCUBA-2 observed Hot DOGs in our sample. The total IR luminosities ($L_{\text{IR}}^{\text{tot}}$), the IR luminosities emitted by the torus (L_{IR}^{t}) and cold dust ($L_{\text{IR}}^{\text{GB}}$) are also listed in Table 2. We can find that the derived $L_{\text{IR}}^{\text{tot}}$ are independent on the adopted models. The average difference of the total IR luminosities between the CLUMPY+GB model and the Two-phase+GB model is only 0.06 dex. However, the relative contributions of L_{IR}^{t} and $L_{\text{IR}}^{\text{GB}}$ to $L_{\text{IR}}^{\text{tot}}$ change a bit. Four out of ten Hot DOGs can be fitted with a sole two-phase torus model, while the rest of them require a cold dust component, contributing up to 30% of the total IR luminosities. The average fraction of the cold dust to the total IR luminosities is 8%, which is only one third of the fraction with the CLUMPY+GB model (see Figure 3). In Figure 4, we plot the one-dimensional and two-dimensional marginalized posterior probability distributions of IR luminosities of the torus (L_{IR}^{t}) and cold dust ($L_{\text{IR}}^{\text{GB}}$) components, for W2201+0226 as an example. We can find that both L_{IR}^{t} and $L_{\text{IR}}^{\text{GB}}$ have been constrained to a narrower range using the CLUMPY+GB model than using the Two-phase+GB model.

We employ a gray body model to represent the cold dust emission, which is defined in Equation 1 by assuming general opacity. The cold dust temperature T_{dust} of each Hot DOG has been derived if a gray body component is required. In the CLUMPY+GB model, the derived dust temperatures range from 42 K to 91 K, with a mean value of 68 K. As a comparison, the derived dust temperatures in the Two-phase+GB model range from 36 K to 74 K, with a mean value of 56 K.

One of the advantages of BayeSED code is that we can compare different models quantitatively by deriving their Bayesian evidences (Jeffreys 1998; Gregory 2005), which represent a practical implementation of the Occam's razor principle. In Table 3, we present the natural logarithm $\ln(\text{ev}_{\text{CLUMPY+GB}})$ and $\ln(\text{ev}_{\text{Two-phase+GB}})$ of the Bayesian evidences for CLUMPY+GB and Two-phase+GB models. We also present the natural logarithm of Bayes factor $\ln\left(\frac{\text{ev}_{\text{CLUMPY+GB}}}{\text{ev}_{\text{Two-phase+GB}}}\right)$ in Table

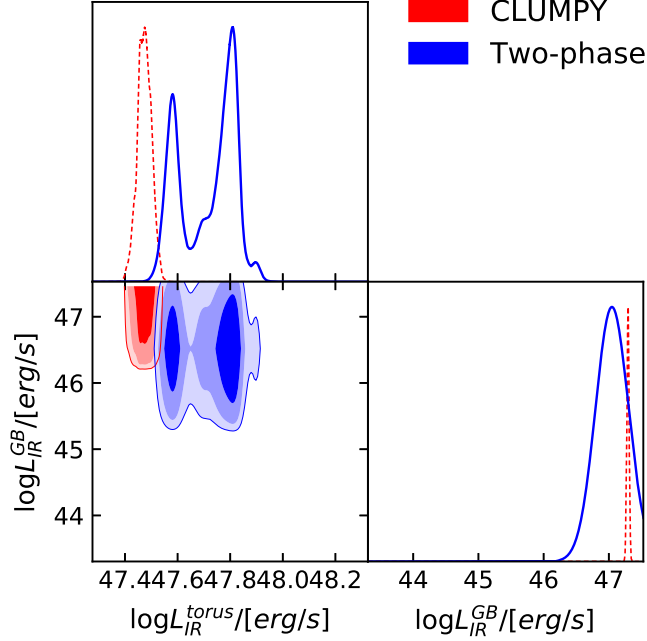


Figure 4. One-dimensional and two-dimensional marginalized posterior probability distributions of IR luminosities of the torus (L_{IR}^{t}) and cold dust ($L_{\text{IR}}^{\text{GB}}$) components, for W2201+0226 as an example. The color coding represents the confidence levels. Both one-dimensional and two-dimensional marginalized posterior probability distributions have been normalized to unit area. Red and blue colors mark the CLUMPY+GB model and the Two-phase+GB model, respectively.

3. We find that the CLUMPY+GB model has the higher Bayesian evidence than the Two-phase+GB model for all Hot DOGs. We also find that eight out of ten Hot DOGs have $\ln\left(\frac{\text{EV}_{\text{CLUMPY+GB}}}{\text{EV}_{\text{Two-phase+GB}}}\right) > 10$ (corresponding to odds of $> 20000 : 1$), which represent strong evidence in favor of CLUMPY+GB model according to the empirically calibrated Jeffreys’s scale (Jeffreys 1961; Trotta 2008). This result indicates that the cold dust component in Hot DOGs may be non-negligible.

4.2. Environments around Hot DOGs

Hot DOGs have been found to live in dense environments by previous works (Jones et al. 2014; Assef et al. 2015; Jones et al. 2015; Silva et al. 2015). Fourteen and five submillimeter serendipitous sources in the 10 SCUBA-2 fields around Hot DOGs have been detected at greater than 3σ and 3.5σ , respectively (see Figure 5 and Table 4). As indicated by the Equation 7 in Geach et al. (2017), the false detection rate of SCUBA-2 $850 \mu\text{m}$ observations is a function of signal-to-noise ratio. The false

Table 3. The Bayesian evidences of "CLUMPY+GB" and "Two-phase+GB" models

Source	$\ln(\text{ev}_{\text{CLUMPY+GB}})$	$\ln(\text{ev}_{\text{Two-phase+GB}})$	$\ln\left(\frac{\text{ev}_{\text{CLUMPY+GB}}}{\text{ev}_{\text{Two-phase+GB}}}\right)$
W0126-0529	-145.56 ± 0.32	-210.03 ± 0.27	64.47 ± 0.58
W0134-2922	-77.97 ± 0.20	-100.19 ± 0.20	22.23 ± 0.40
W0248+2705	-71.88 ± 0.17	-87.45 ± 0.18	15.57 ± 0.35
W0422-1028	-71.84 ± 0.18	-93.43 ± 0.20	21.59 ± 0.38
W0757+5113	-69.94 ± 0.17	-84.46 ± 0.24	14.52 ± 0.42
W0859+4823	-94.29 ± 0.19	-112.32 ± 0.20	18.03 ± 0.40
W1248-2154	-69.40 ± 0.18	-76.50 ± 0.24	7.10 ± 0.42
W1838+3429	-41.46 ± 0.17	-44.85 ± 0.20	3.39 ± 0.38
W2201+0226	-87.25 ± 0.21	-104.50 ± 0.22	17.25 ± 0.43
W2210-3507	-99.27 ± 0.20	-118.57 ± 0.26	19.30 ± 0.46

detection rate is about 60% at the $> 3\sigma$ level and falls to about 20% at 3.5σ limit. We calculate the cumulative source counts $N(> S_{850\mu\text{m}})$ for the submillimeter serendipitous sources with a $S/N > 3.5$ by following the method described in [Ono et al. \(2014\)](#) and [Silva et al. \(2015\)](#). We estimate the deboosted flux densities by correcting the flux boosting using the Equation 5 in [Geach et al. \(2017\)](#).

In Figure 6, we plot our result (red circle) and compare it with those in the previous results around Hot DOGs, the blank field survey and expected from models. We include the counts around 30 radio-selected Hot DOGs (gray diamonds) from [Jones et al. \(2015\)](#) and 10 WISE-selected Hot DOGs (red triangle) from [Jones et al. \(2014\)](#). Both samples used to estimate number counts have been selected from [Jones et al. \(2017\)](#) with $S/N > 3.5$. We overplot the number counts of SCUBA-2 850 μm sources determined by [Geach et al. \(2017\)](#) in SCUBA-2 Cosmology Legacy Survey (S2CLS, blue squares) and the models of [Cai et al. \(2013\)](#) and [Lacey et al. \(2016\)](#). Considering the uncertainties, our count is consistent with the counts obtained by [Jones et al. \(2015\)](#). Relative to blank fields and model expectations, the number counts of SMGs around Hot DOGs imply an excess of ~ 6 times.

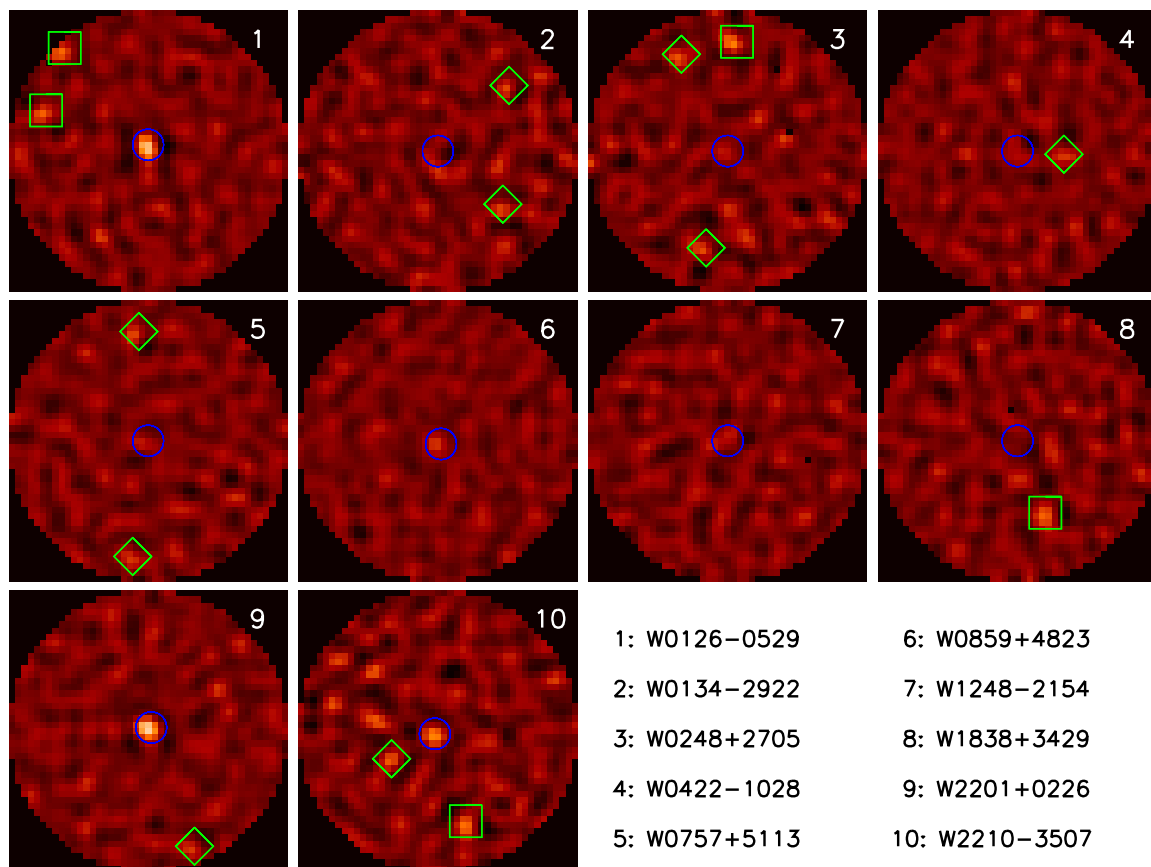


Figure 5. SCUBA-2 $850\mu\text{m}$ 1.5-arcminute-radius maps of the ten Hot DOGs in our sample. The circles mark the position of the WISE detections of Hot DOGs. Serendipitous sources brighter than 3σ and 3.5σ are shown by diamonds and squares, respectively. In total, 14 serendipitous sources at $> 3\sigma$ have been detected, while the number falls to 5 at $> 3.5\sigma$ level. Having a good sensitivity, [Jones et al. \(2014\)](#) found 17 and 7 serendipitous sources at $> 3\sigma$ and $> 3.5\sigma$ around 10 Hot DOGs, respectively.

5. DISCUSSION

Combined with other IR data, our SCUBA-2 follow-up observations of ten Hot DOGs show that they have very high IR luminosities and cold dust temperatures. Hot DOGs are brighter by an order of magnitude than other IR luminous galaxies, such as SMGs and DOGs, but they have the comparable bolometric luminosities to the most luminous QSOs in the Universe ([Assef et al. 2015](#)). Our IR SED decomposition of Hot DOGs suggests that most of their IR radiations are from AGN tori, which are heated by the black-hole accretion. This result confirms again that Hot DOGs are in fact the luminous, dust-obscured QSOs. Despite the dominance of AGN torus component, most

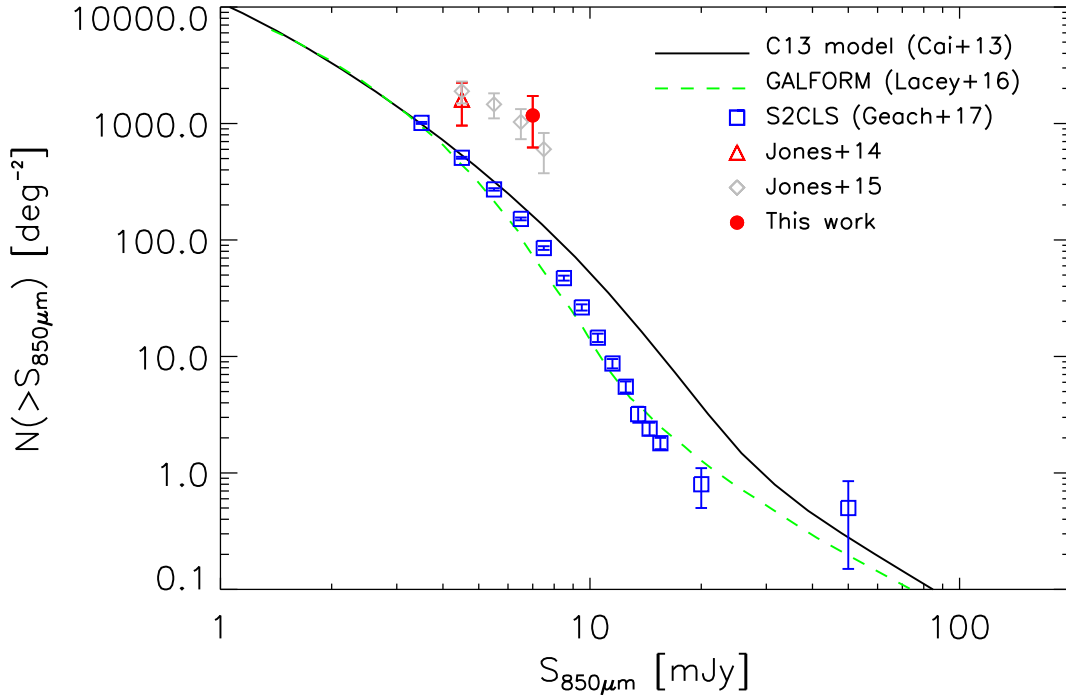


Figure 6. The cumulative number count of SMGs around 10 Hot DOGs (red circle) obtained with SCUBA-2 observations at $850\ \mu\text{m}$ with a $S/N > 3.5$. We also plot the SCUBA-2 counts around 30 radio-selected Hot DOGs (gray diamonds) from Jones et al. (2015) and 10 WISE-selected Hot DOGs (red triangle) from Jones et al. (2014). We overplot the number counts of SCUBA-2 $850\ \mu\text{m}$ sources determined by Geach et al. (2017) in the S2CLS survey (blue squares) and the models of Cai et al. (2013) and Lacey et al. (2016).

of Hot DOGs still require a non-negligible cold dust component, suggesting a co-existing starburst activity. Our recent ALMA CO observations of three Hot DOGs reveal that they have a significant molecular gas reservoir ($\sim 10^{10-11} M_{\odot}$) which can provide the required fuel for both extreme star formation and black-hole accretion (Fan et al. 2017, in prep).

The cold dust temperature T_{dust} depends on the adopted torus and gray body models in the IR SED decomposition. The choice of torus model will affect both the derived temperature and IR luminosity of cold dust. Adopting CLUMPY torus model, we derive the higher values of T_{dust} and $L_{\text{IR}}^{\text{GB}}$ (see Table 2 and Figure 7). For six Hot DOGs having the SED decomposition results with both torus models, the derived $\log L_{\text{IR}}^{\text{GB}}$ and T_{dust} using the CLUMPY+GB model are on average 0.2 dex and 12 K higher than those derived using the Two-phase+GB model, respectively. The difference

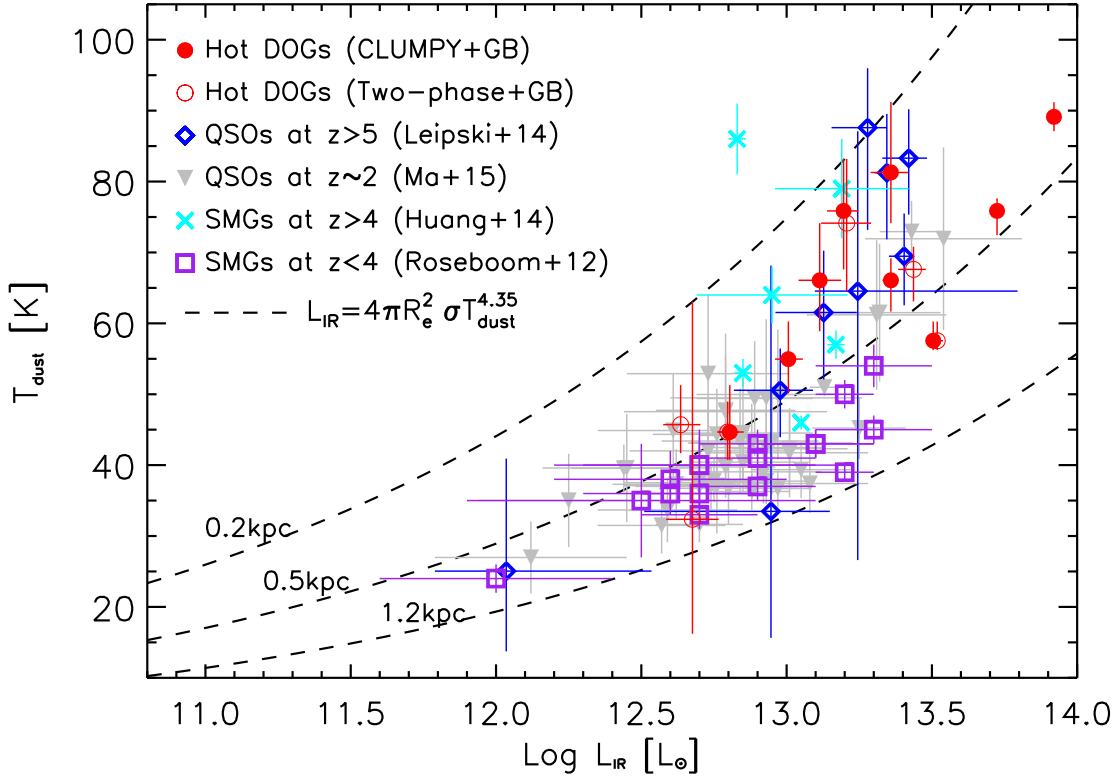


Figure 7. Temperature (T_{dust}) versus IR luminosity ($L_{\text{IR}}^{\text{GB}}$) of cold dust in Hot DOGs derived by our IR SED decomposition with CLUMPY+GB model (filled circles) and Two-phase+GB model (open circles), respectively. We also plot the results of other high-redshift populations: QSOs at $z > 5$ (diamonds; Leipski et al. 2014) and at $z \sim 2$ (upside down triangles; Ma & Yan 2015), SMGs at $z > 4$ (crosses; Huang et al. 2014) and at $z < 4$ (squares; Roseboom et al. 2012). Dashed lines represent the expected $T_{\text{dust}} - L_{\text{IR}}^{\text{GB}}$ relation of a gray body with different effective radius values (0.2, 0.5 and 1.2 kpc). The future high-resolution dust continuum observations by ALMA will provide further insights.

may raise from the truth that two torus models adopt the different dust particles and torus geometry. The starburst contribution to the far IR emission can well be marginal in the Two-phase+GB model, which is consistent with the result in Siebenmorgen et al. (2015). In Equation 1, we assume general opacity. As discussed in our previous work (Fan et al. 2016b), the derived cold dust temperature of Hot DOGs adopting general opacity is averagely ~ 20 K higher than that under the optically thin assumption. This trend also exists in other high-redshift IR luminous galaxies (Conley et al. 2011; Magdis et al. 2012). However, the derived cold dust temperature of our Hot DOGs is about 56 K

Table 4. Number of serendipitous sources and negative peaks in each map at greater than 3σ and 3.5σ , respectively.

Source	Number of		Number of	
	serendipitous sources		negative peaks	
	$> 3\sigma$	$> 3.5\sigma$	$> 3\sigma$	$> 3.5\sigma$
W0126–0529	2	2	1	1
W0134–2922	2	0	0	0
W0248+2705	3	1	3	0
W0422–1028	1	0	1	0
W0757+5113	2	0	3	0
W0859+4823	0	0	1	1
W1248–2154	0	0	0	0
W1838+3429	1	1	0	0
W2201+0226	1	0	0	0
W2210–3507	2	1	0	0

adopting the optically thin assumption, which is still higher than those found in other high-redshift IR luminous galaxies (Magdis et al. 2010; Magnelli et al. 2012; Melbourne et al. 2012).

In Figure 7, we plot the derived dust temperature as a function of IR luminosity for our Hot DOGs. We also plot the $T_{\text{dust}} - L_{\text{IR}}$ relation of other high-redshift populations as a comparison, including QSOs at $z > 5$ (diamonds; Leipski et al. 2014) and at $z \sim 2$ (upside down triangles; Ma & Yan 2015), SMGs at $z > 4$ (crosses; Huang et al. 2014) and at $z < 4$ (squares; Roseboom et al. 2012). We use a modified Stefan-Boltzmann law ($L_{\text{IR}} = 4\pi R_e^2 \sigma T^{4.35}$) to describe $T_{\text{dust}} - L_{\text{IR}}$ relation of a gray body (Symeonidis et al. 2013; Ma & Yan 2015; Fan et al. 2016b). As seen in Figure 7, Hot DOGs have hotter dust temperature than SMGs. The higher dust temperature in our Hot DOGs may be due to two aspects: their high IR luminosity L_{IR} and/or their small effective radius of the

equivalent FIR-emitting region (R_e), as suggested by the expected $T_{\text{dust}} - L_{\text{IR}}$ relation of a gray body (dashed lines in Figure 7). The future ALMA high-resolution dust continuum observations will provide further insights by comparing the FIR-emitting sizes of Hot DOGs and SMGs. Compared to UV-selected QSOs with similar IR luminosity, Hot DOGs have the same dust temperature range, confirming the idea that Hot DOGs are the luminous dust-obscured QSOs.

By counting the submillimeter serendipitous sources around Hot DOGs and estimating their cumulative number counts, we find that Hot DOGs live in dense environments (see Figure 5,6). The result is consistent with the previous works. Jones et al. (2014) found evidence of an overdensity of sub-mm neighbors to a small sample of HotDOGs using 850 μm observations with SCUBA-2 at JCMT. Assef et al. (2015) studied the environments of HotDOGs using the deep Warm Spitzer IRAC imaging. They showed that the number of red galaxies within 1 arcminute radius is significantly above the number observed in random pointing. And their environments are as dense as those of the clusters identified by the Clusters Around Radio-loud AGN survey (CARLA). Using the Atacama Large Millimeter/Sub-millimeter Array (ALMA) 345 GHz images, Silva et al. (2015) also found an overdensity of SMGs around radio-selected, Hot DOGs at $z \sim 2$. The results are not surprising, given the extremely high luminosity and stellar mass ($> 10^{11} M_{\odot}$) of HotDOGs (Assef et al. 2015; Lonsdale et al. 2015). Frey et al. (2016) performed exploratory high-resolution 1.7-GHz observations of a small sample of four Hot DOGs with the European VLBI Network (EVN). The high-resolution radio structures, the component separations and radio powers support that QSOs residing in Hot DOGs may be genuine young radio sources where starburst and QSO activities coexist. This result leads to the speculation that Hot DOGs could be the earlier evolutionary phase of radio-loud QSOs, which are preferentially located in high-redshift protoclusters (Wylezalek et al. 2013; Hatch et al. 2014). In order to study the environments of HotDOGs thoroughly, we are proposing to search Lyman alpha emitters (LAEs) around them. As the narrow-band imaging can constrain the redshift of the objects to the small range, LAEs are very useful in studying the spatial distribution of the star-forming galaxies at high redshift. In the recent decade, targeted searches using narrow-band imaging for high-redshift rich environments around powerful high-redshift radio galaxies (HzRGs)

have proven very successful (Venemans et al. 2007; Matsuda et al. 2011). Our ongoing studies will not only provide a direct evidence for (or against) whether Hot DOGs could be a good tracer of high-redshift galaxy structure, but also provide an insight to whether their extreme starburst and AGN activities are related to their environments.

6. SUMMARY

Our main results from JCMT SCUBA-2 850 μm follow-up of 10 Hot DOGs are summarized as follows.

1. The IR SED of Hot DOGs in our sample can be fitted by a combination of AGN torus and cold dust components. The derived total IR luminosities of Hot DOGs are extremely high and independent of the choice of torus model. Most of them are ELIRGs with $L_{\text{IR}}^{\text{tot}} > 10^{14} L_{\odot}$.
2. The torus emissions dominate the total IR energy output, regardless of the choice of torus model. The derived cold dust contribution depends on the adopted torus model. If adopting the Two-phase+GB model, the average fraction of the cold dust to the total IR luminosity is about 8%, which is only one third of the fraction with the CLUMPY+GB model. We compare two models quantitatively by deriving their Bayesian evidences. We find that the CLUMPY+GB model has the significantly higher Bayesian evidence than the Two-phase+GB model for all Hot DOGs, which represent strong evidence in favor of CLUMPY+GB model. This result indicates that the cold dust component in Hot DOGs may be non-negligible.
3. The derived cold dust temperatures in Hot DOGs are on average 68 K (56 K) using the CLUMPY+GB model (Two-phase+GB model), which are comparable to those in QSOs with similar IR luminosity, but much higher than those in SMGs. Higher dust temperatures in Hot DOGs may be due to the more intense radiation field caused by intense starburst and obscured AGN activities.
4. We count the submillimeter serendipitous sources around Hot DOGs and estimate their cumulative number counts at $> 3.5\sigma$ level. The number counts of SMGs around Hot DOGs imply

an excess of ~ 6 times relative to blank fields and model expectations. The result confirms the previous argument that Hot DOGs may lie in dense environments. Future studies with narrow-band imaging may increase our insight on their environments.

5. All of our results support the scenario in which Hot DOGs are luminous, dust-obscured QSOs, linking extreme starburst and UV-bright QSOs.

The authors would like to thank the anonymous referee for his/her comments and suggestions, which have greatly improved this paper. LF acknowledges the support from National Key Research and Development Program of China (No. 2017YFA0402703). This work is supported by the National Natural Science Foundation of China (NSFC, Nos. 11433005, 11773063 and 11773020) and Shandong Provincial Natural Science Foundation, China (ZR2017QA001). KK acknowledges the Knut and Alice Wallenberg Foundation for support.

The James Clerk Maxwell Telescope is operated by the East Asian Observatory on behalf of The National Astronomical Observatory of Japan, Academia Sinica Institute of Astronomy and Astrophysics, the Korea Astronomy and Space Science Institute, the National Astronomical Observatories of China and the Chinese Academy of Sciences (Grant No. XDB09000000), with additional funding support from the Science and Technology Facilities Council of the United Kingdom and participating universities in the United Kingdom and Canada.

Facility: WISE, Herschel (PACS,SPIRE), JCMT (SCUBA-2).

REFERENCES

- | | |
|--|---|
| Alexander, D. M., & Hickox, R. C. 2012, <i>New Astronomy Reviews</i> , 56, 93 | Beelen, A., Cox, P., Benford, D. J., et al. 2006, <i>ApJ</i> , 642, 694 |
| Assef, R. J., Eisenhardt, P. R. M., Stern, D., et al. 2015, <i>ApJ</i> , 804, 27 | Blain, A. W., Smail, I., Ivison, R. J., Kneib, J.-P., & Frayer, D. T. 2002, <i>PhR</i> , 369, 111 |
| Assef, R. J., Walton, D. J., Brightman, M., et al. 2016, <i>ApJ</i> , 819, 111 | Brandt, W. N., & Alexander, D. M. 2015, <i>A&A Rv</i> , 23, 1 |

- Bridge, C. R., Blain, A., Borys, C. J. K., et al. 2013, *ApJ*, 769, 91
- Cai, Z.-Y., Lapi, A., Xia, J.-Q., et al. 2013, *ApJ*, 768, 21
- Casey, C. M., Narayanan, D., & Cooray, A. 2014, *PhR*, 541, 45
- Chapin, E. L., Berry, D. S., Gibb, A. G., et al. 2013, *MNRAS*, 430, 2545
- Conley, A., Cooray, A., Vieira, J. D., et al. 2011, *ApJL*, 732, L35
- Cutri, R. M., & et al. 2013, *VizieR Online Data Catalog*, 2328, 0
- Dempsey, J. T., Friberg, P., Jenness, T., et al. 2013, *MNRAS*, 430, 2534
- Dey, A., Soifer, B. T., Desai, V., et al. 2008, *ApJ*, 677, 943
- Díaz-Santos, T., Assef, R. J., Blain, A. W., et al. 2016, *ApJL*, 816, L6
- Eisenhardt, P. R. M., Wu, J., Tsai, C.-W., et al. 2012, *ApJ*, 755, 173
- Fan, L., Han, Y., Fang, G., et al. 2016, *ApJL*, 822, L32
- Fan, L., Han, Y., Nikutta, R., Drouart, G., & Knudsen, K. K. 2016, *ApJ*, 823, 107
- Farrah, D., Petty, S., Connolly, B., et al. 2017, *arXiv:1705.02649*
- Feroz, F., & Hobson, M. P. 2008, *MNRAS*, 384, 449
- Feroz, F., Hobson, M. P., & Bridges, M. 2009, *MNRAS*, 398, 1601
- Frey, S., Paragi, Z., Gabányi, K. É., & An, T. 2016, *MNRAS*, 455, 2058
- Geach, J. E., Dunlop, J. S., Halpern, M., et al. 2017, *MNRAS*, 465, 1789
- Gregory, P. 2005, *Bayesian Logical Data Analysis for the Physical Sciences* (New York, NY, USA: Cambridge University Press)
- Griffin, M. J., Abergel, A., Abreu, A., et al. 2010, *A&A*, 518, L3
- Han, Y., & Han, Z. 2012, *ApJ*, 749, 123
- Han, Y., & Han, Z. 2014, *ApJS*, 215, 2
- Holland, W. S., Bintley, D., Chapin, E. L., et al. 2013, *MNRAS*, 430, 2513
- Hopkins, P. F., Hernquist, L., Cox, T. J., & Kereš, D. 2008, *ApJS*, 175, 356
- Hatch, N. A., Wylezalek, D., Kurk, J. D., et al. 2014, *MNRAS*, 445, 280
- Huang, J.-S., Rigopoulou, D., Magdis, G., et al. 2014, *ApJ*, 784, 52
- Jeffreys, H. 1961, *The Theory of Probability* Oxford Classics Series (3rd ed.; Oxford: Oxford Univ. Press)
- Jeffreys, H. 1998, *The Theory of Probability* (OUP Oxford)
- Jones, S. F., Blain, A. W., Stern, D., et al. 2014, *MNRAS*, 443, 146
- Jones, S. F., Blain, A. W., Lonsdale, C., et al. 2015, *MNRAS*, 448, 3325
- Jones, S. F., Blain, A. W., Assef, R. J., et al. 2017, *MNRAS*, 469, 4565
- Komatsu, E., Smith, K. M., Dunkley, J., et al. 2011, *ApJS*, 192, 18
- Kormendy, J., & Ho, L. C. 2013, *ARA&A*, 51, 511

- Lacey, C. G., Baugh, C. M., Frenk, C. S., et al. 2016, *MNRAS*, 462, 3854
- Leipski, C., Meisenheimer, K., Walter, F., et al. 2014, *ApJ*, 785, 154
- Lonsdale, C. J., Lacy, M., Kimball, A. E., et al. 2015, *ApJ*, 813, 45
- Ma, Z., & Yan, H. 2015, *ApJ*, 811, 58
- Magdis, G. E., Daddi, E., Béthermin, M., et al. 2012, *ApJ*, 760, 6
- Magdis, G. E., Elbaz, D., Hwang, H. S., et al. 2010, *MNRAS*, 409, 22
- Magnelli, B., Lutz, D., Santini, P., et al. 2012, *A&A*, 539, A155
- Matsuda, Y., Smail, I., Geach, J. E., et al. 2011, *MNRAS*, 416, 2041
- Melbourne, J., Soifer, B. T., Desai, V., et al. 2012, *AJ*, 143, 125
- Nenkova, M., Ivezić, Ž., & Elitzur, M. 2002, *ApJL*, 570, L9
- Nenkova, M., Sirocky, M. M., Ivezić, Ž., & Elitzur, M. 2008a, *ApJ*, 685, 147
- Nenkova, M., Sirocky, M. M., Nikutta, R., Ivezić, Ž., & Elitzur, M. 2008b, *ApJ*, 685, 160
- Ono, Y., Ouchi, M., Kurono, Y., & Momose, R. 2014, *ApJ*, 795, 5
- Piconcelli, E., Vignali, C., Bianchi, S., et al. 2015, *A&A*, 574, L9
- Pilbratt, G. L., Riedinger, J. R., Passvogel, T., et al. 2010, *A&A*, 518, L1
- Poglitsch, A., Waelkens, C., Geis, N., et al. 2010, *A&A*, 518, L2
- Reddy, N. A., Steidel, C. C., Pettini, M., et al. 2008, *ApJS*, 175, 48
- Ricci, C., Assef, R. J., Stern, D., et al. 2017, *ApJ*, 835, 105
- Roseboom, I. G., Ivison, R. J., Greve, T. R., et al. 2012, *MNRAS*, 419, 2758
- Sanders, D. B., Soifer, B. T., Elias, J. H., et al. 1988, *ApJ*, 325, 74
- Sanders, D. B., & Mirabel, I. F. 1996, *ARA&A*, 34, 749
- Siebenmorgen, R., Heymann, F., & Efstathiou, A. 2015, *A&A*, 583, A120
- Silva, A., Sajina, A., Lonsdale, C., & Lacy, M. 2015, *ApJL*, 806, L25
- Stern, D., Lansbury, G. B., Assef, R. J., et al. 2014, *ApJ*, 794, 102
- Symeonidis, M., Vaccari, M., Berta, S., et al. 2013, *MNRAS*, 431, 2317
- Trotta, R. 2008, *ConPh*, 49, 71
- Tsai, C.-W., Eisenhardt, P. R. M., Wu, J., et al. 2015, *ApJ*, 805, 90
- Venemans, B. P., Röttgering, H. J. A., Miley, G. K., et al. 2007, *A&A*, 461, 823
- Wang, R., Wagg, J., Carilli, C. L., et al. 2008, *AJ*, 135, 1201
- Wang, R., Wagg, J., Carilli, C. L., et al. 2011, *AJ*, 142, 101
- Wright, E. L., Eisenhardt, P. R. M., Mainzer, A. K., et al. 2010, *AJ*, 140, 1868
- Wu, J., Tsai, C.-W., Sayers, J., et al. 2012, *ApJ*, 756, 96

Wu, J., Bussmann, R. S., Tsai, C.-W., et al. 2014,
ApJ, 793, 8

Wu, J., Jun, H. D., Assef, R. J., et al. 2017,
arXiv:1703.06888

Wylezalek, D., Galametz, A., Stern, D., et al.
2013, ApJ, 769, 79